The Environmental Impacts of Marine Mining

- Michael Anthony Metford Saunders -

--

This work is dedicated to my Granddad, Terry 'Grumpy' White,
whose curiosity in geological sciences has inspired me for as long as I can remember.

Since studying Geological Oceanography, he's only understood half of my work.

--

Dissertation, as supervised by Katrien van Landegham, Bangor University

Abstract

This work parameterises and quantifies generalised abiotic environmental impacts of anthropogenically created sediment plumes, and details effects of accelerated oxidative dissolution to the seabed environment, due to "marine hydrothermal deposit" mining. These resources will soon contribute to supplying growing and diversifying demands for metals when Nautilus Minerals Incorporated commence their Solwara 1 project in late 2019.

Using the operational design for Solwara 1, in the Bismarck Sea (near Papua New Guinea), and analysing particle dynamics, mineralogical, chemical and physical oceanographical data: this work introduces and formulates the Potential Impact Range and Potential Impact Intensity, within a user-defined Potential Impact Timeframe.

The limitations of the scientific communities' understanding and potential shortfalls of existing Environmental Impact Assessments are identified. Included in this work is a MATLAB script to estimate the impact range and intensity given a user-defined timeframe.

Contents

List of Figures

List of Tables

Introduction [A]

i. Defining This Work

"*If it cannot be grown, it has to be mined"* (*eg.* Camborne School of Mines, 2013).

The function of the mining industry is to explore and exploit geological resources, then to process and enrich the materials for use in industry and wider society: this definition is inclusive of bulk and petroleum resource mining. Hereinto, as per the scope of this work, 'mining' refers to the exploration, exploitation and enrichment of metalliferous minerals and ore bodies. This work focuses on exploitation and dewatering the metalliferous resource.

The mining industry has been close to 'dipping its toes into the water' for a decade. Recent times have seen literature on the marine mining typically falling into three regions: technical papers on specific concerns, often drawing from lessons learnt in conventional mining or the petroleum industry (*e.g.* Fallon, et al., 2017; Van Wijk, 2016); investor reports on the state of the operational design (*e.g.* Gwyther, 2008a; Gwyther, 2008b); or qualitative papers on ecological threats associated by marine mining (*e.g.* Brown & Hauton, 2018). These works are often project specific, though a quantitative overview of physical parameters to predict the range and intensity of environmental impact is very limited.

This dissertation aims to conceptually parameterise and estimate the physical and chemical changes to environments surrounding marine hydrothermal deposits (MHDs) caused by 'marine mining'; and highlight limitations in existing evaluations.

ii. The Premise of Marine Mining

Copper, a highly applicable industry metal, is prospected for in both marine and conventional mining: primary analysis presented in this work justifies the focus on copper and copper ores (sulphides), finding topical comparisons between marine and terrestrial deposits.

Consider technological revolutions, times where the diversification and usage of metals increase. The fifty years prior to the Industrial Revolution, 1780-1880 (Šmihula, 2011), can be considered alike to today: Pryce (1778) compiled data over decades prior to the industrial revolution, and records the increase in British copper production, prior to the "modern" mining age. This data (tonne per year) is presented in Figure 1.

Exponential growth is observed. Given a coefficient of regression 0.8222, for the equation:

$$\boldsymbol{y = (4 \times 10^{-24}) e^{0.036x}}$$

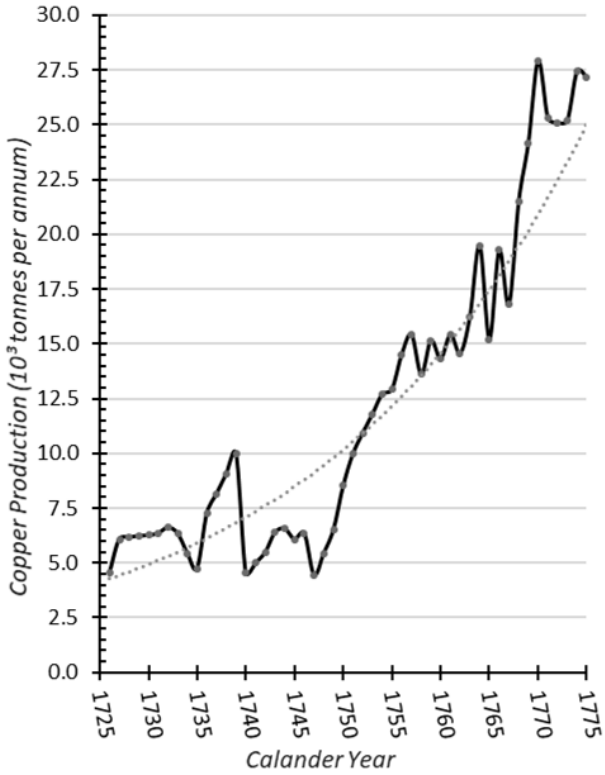

Figure 1: Graph of exponential Copper production prior to the industrial revolution (Pryce, 1778).

A similar situation is seen these past twenty to twenty-five years, as society is similarly on the cusp of a "post-information and telecommunications revolution", forwarding technologies as "bio- medicine, nanotechnology and alternative fuels" (Šmihula, 2011).

Figure 2 presents the same analysis of global change in copper usage (●, tonne per year) since 1960, (data extracted from International Copper Study Group (2017)). This data is coupled with human population (▲) since 1960 (extracted from Department of Economic and Social Affairs: Population Division (2017)): allowing for further analysis for copper usage per person since 1960.

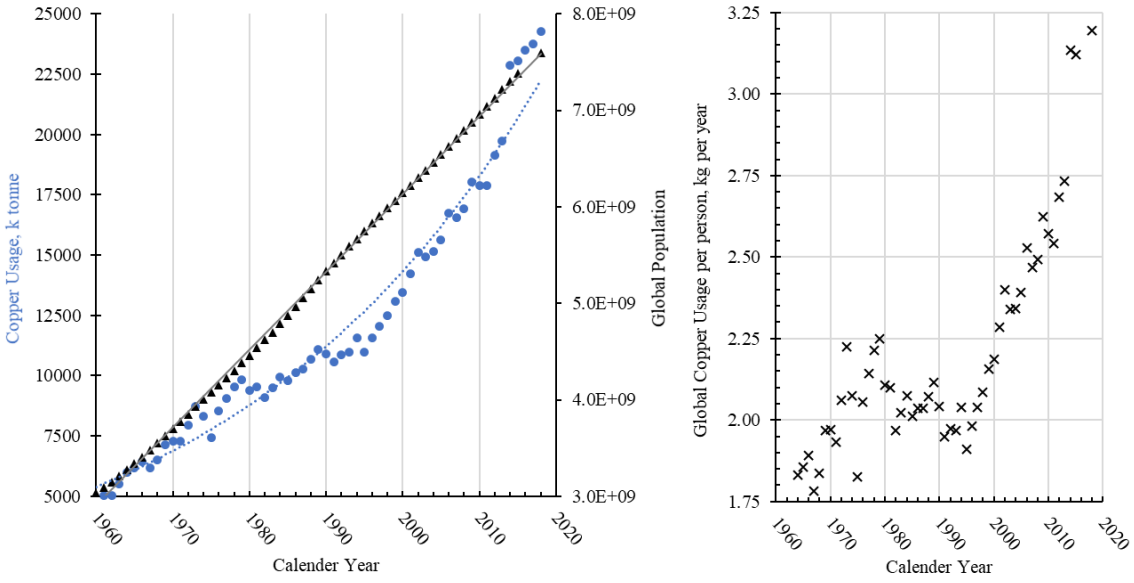

Figure 2: [left] Global copper usage (ICSG, 2017) and world population by year (Department of Economic and Social Affairs: Population Division, 2017). [Right] Global copper usage per person, as quotient of usage and population.

Global copper usage in 1960 was approximately 165 times that of the beginning of the industrial revolution. Since 1960, a very strong ($R^2 = 0.971$) exponential growth ($y = 8.0\times10^{-18}\, e^{0.0244x}$) is exhibited, as in Figure 2. Growth of global human population has increased linearly ($y = 8.0\times10^{7}x - 2\times10^{11}$; $R^2 = 0.9991$) trend.

As for usage per person: three trends are observed, the last of which, is since 1995. This section has a strong ($R^2 = 0.921$) linear growth ($y = 0.0516x - 100.98$) in demand per person.

iii. Materials Crisis and Marine Solutions

A growing demand for Copper, among many other metals, now places the mining industry in crisis. Fundamentally, the role of mining is to 'fill the gap between recycled supply, and demand' and that 'easy' resources are exhausted as more challenging (thus lower profit) resources are left (Jeswiet, 2017). The issue arises when there are no 'easy' resources left. Even more troubling is the diversification of metal demand, into rare materials including Lathanum, Gold and Platinum Group Metals (PGM), which are increasingly used in technology and industry. For example, the average modern mobile phone contains 62 different elements, of the 83 which are stable (Desjardens, 2016).

Figure 3 shows the relative abundances of elements to 10^6 Si atoms in continental crust (Haxel, et al., 2002). Although, given the principle differences in continental and oceanic crust, the composition elements in marine settings are often not reflective of their land counterparts.

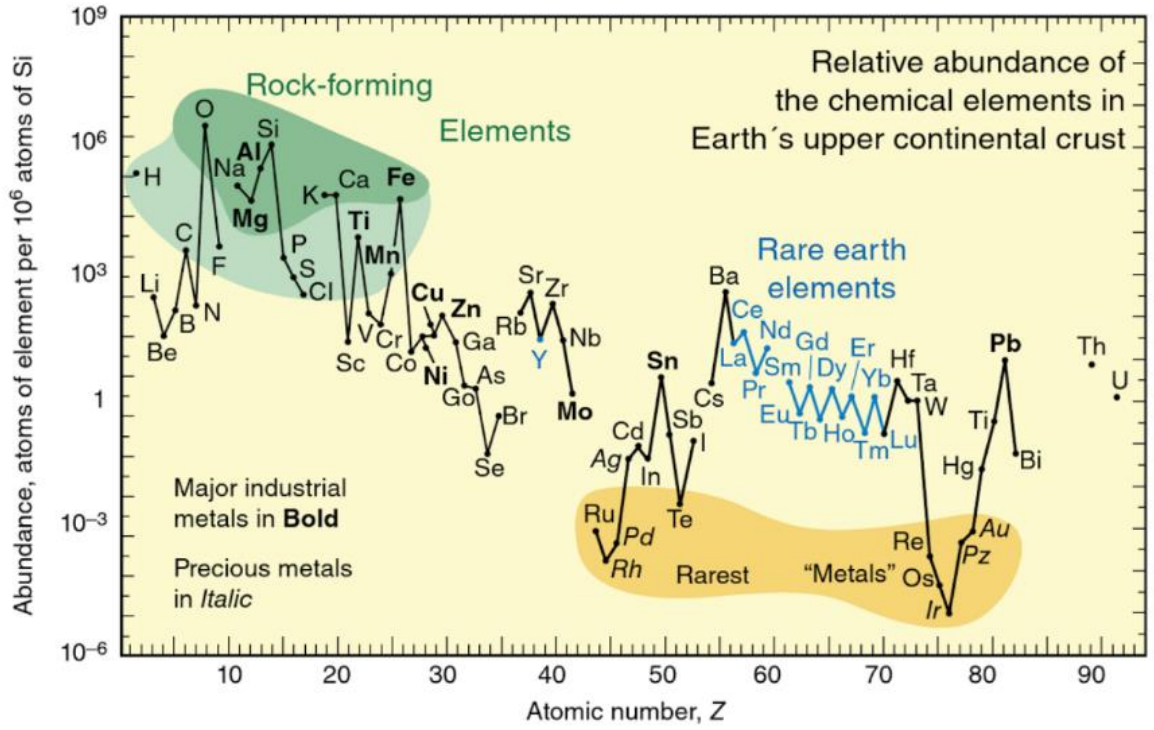

Figure 3: USGS schematic of elemental abundances in continental crusts, per 10^6 Si atoms. (Haxel, et al., 2002)

Typically, marine hydrothermal systems host metal deposits in the order of 1-5 megatonnes, which are much smaller than terrestrially mined desposits of typically 50-60 megatonnes

(Hoagland, et al., 2010). These marine deposits are at notably higher concentration than their land counterparts, and exist at the surface: which is an attractive opportunity for prospecters.

- Solwara 1 [Nautilus Minerals], at an average seabed depth of 1550m (Lowe, 2012), is estimated to have an inferred Copper concentration of 6.8% [massive sulphide], 11% [chimney] and 4.5% [lithified sediment]. In addition to 6.5%, 17% and 5.2% Gold respectively. The 'profit-proof-of-concept' site is estimated to yield 1.3 megatonnes of raw material in total (Gwyther, 2008b).

- Grasberg, Indonesia [Freeport McMoRan Inc.] is one of the most productive Gold mines worldwide. (Andres, 2013). The site also produces Copper, at a mean concentration of 0.91% by weight. Gold mean concentration is 0.0000068% wt. However, Copper production is recorded as 482,170 tonnes and Gold at 30,080 tonnes in 2016, from tunnels up to approximately 0.6km depth (Freeport McMoRan, 2016).

For means of comparison, for the same production of Copper as Grasberg, Solwara 1 would have to be completely exploited 5.7 times over in a single year. Though, there are estimated to be up to 1000 similar seabed systems around the globe, with only around 350 known sites (Hoagland, et al., 2010). Solwara 1 is but a proof of concept.

Many other metals may exist plentifully in marine deposits, which are seldom found on land. For instance, Szamalek, *et al.* (2011) documents high preliminary concentrations of Gold and Platinum, both rare metals: but concedes that lack of data critically hinders the valuation of deposits.

iv. Defining the Deposits

This work discusses Marine Hydrothermal Deposits (MHDs) as the target resource for marine mining: many different ventures, conceptual and operational, do exist outside the scope of this work.

MHDs are formed by the precipitation of minerals from volatile-to-supercritical solutions when released into ambient deep seawater. Figure 4 illustrates two sub-samples from an MHD extracted from the Galápagos Rift Zone on the East Pacific Rise.

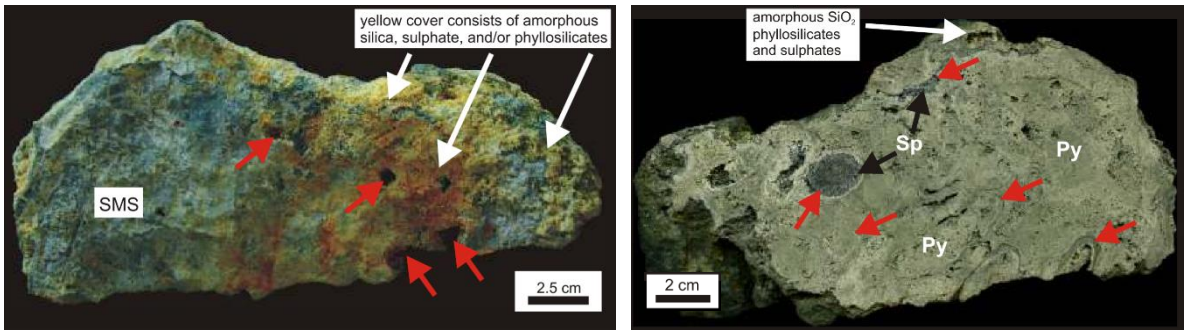

Figure 4: Sample SO39 169GTVB. (left) Active MHD, red arrows indicate open vents. (Right) Mineralized MHD, red arrows indicate former vents, some mineralised with Sphalerite (SP), some Chalcopyrite. Py – Pyrite. (Szamalek, et al., 2011)

Sphalerite and Chalcopyrite forming in mineralized vents: and thus, toward the end of the structures' life cycle (Figure 4 (right) - (Szamalek, et al., 2011)). Further study on the

distribution of metals in relation to time and their mineralisation within deposits may provide data for a more focused mining approach.

The industry, instead, intends to pulverise deposits.

v. Objectives

This work will first discuss the current most feasible operational design for mining epithermal (*i.e.* late-end of life cycle) marine hydrothermal deposits This is widely considered as Nautilus Minerals' Solwara 1 project in the Exclusive Economic Zone (EEZ) of Papua New Guinea. Data on anthropogenically created sediment (ACS) will be extracted and used to parameterise ACS plume dynamics, drawing from particle physics, mineralogical and hydrodynamic studies. Plumes will be considered in both quiescent and dynamic deep-water environments.

Chemical changes due to an increased active surface area of sulphide minerals will be analysed and the challenges this will pose will be discussed.

Methodology **[B]**

i. General Comments

This work uses the diagnostic term Marine Hydrothermal Deposit (MHD) to encapsulate 'black smokers', seabed massive sulphides and polymetallic sulphides. This range of nomenclature appears to be a pitfall in communicating and collating information, the americanisation 'sulfides' often also returns different search results.

ii. Data Acquisition and Analysis

A lack of data is found on the environmental impact. Consequently, this work stipulates on data from the operational design of Solwara 1 (Nautilus Minerals) and applies Stokes Law to the particles, drawing physical parameters from mineralogical properties.

Interpolating conditions of the abiotic environment has allowed analysis of the Potential Impact Range (PIR), using concepts from classical mechanical physics.

Analyses is presented using MATLAB 2016a and 2018a Student (www.mathworks.com/academia), including 2D and 3D plotting. A Fast Fourier Transform (FFT) analysis is included, which resolves the magnitude of frequencies constituting a signal; Inverse FFT resolves frequencies into a signal; and, CUMTRAPZ: in integrating signals.

***Results* [C]**

i) Introducing ACS, Settling Velocities and Solwara 1

The operational design for the aforementioned, Solwara 1, involves a remote-control Seafloor Mining Tool (SMT) which 'cuts' away at the MHD body, using suction to pump matter to a Mining Support Vessel, where matter is dewatered. The return water will then be repumped to approximately 25 to 50 metres above the seabed, driving the Riser and Lift System (RALS). It is expected that return water would contain ACS of nominally <8µm in diameter (*d*), in concentrations up to 6350 mg L^{-1} (Gwyther, 2008a). In the interest of completeness, the minimum relevant grain size is defined as 0.1µm in this work.

Nautilus Minerals expect the RALS to pump water at a rate of 2.4×10^{7} L day^{-1}, assuming continuous (24/7) operation. This equates to 0.28 m^{3} s^{-1} (Gwyther, 2008a). The return water is assumed to be outputted at the same rate.

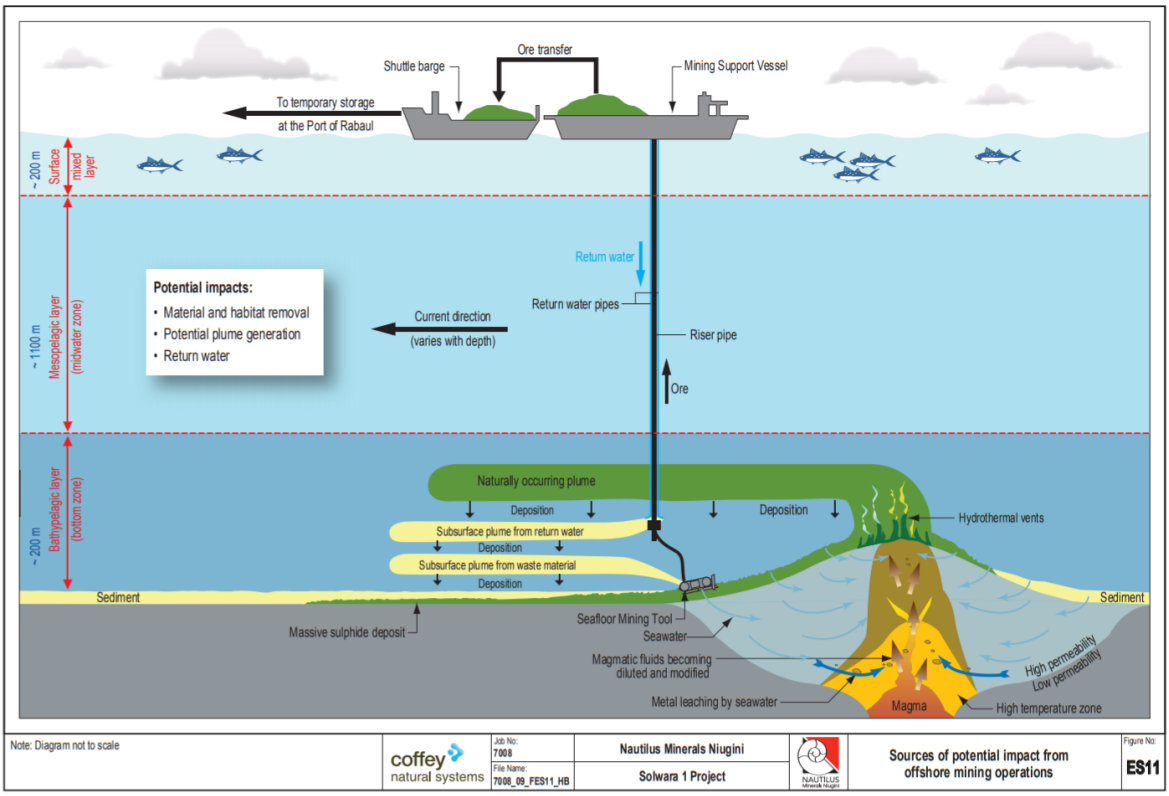

Figure 5: Conceptual schematic of subsurface sediment plumes expected from Solwara 1 operations (Nautilus Minerals Niugini, 2008) (Gwyther, 2008a)

This 8µm ACS, at maximum a very fine silt (Wentworth, 1922), will be the widest implicating ACS due to a low settling velocity, and a position higher in the water column: thus, being easily kept in suspension and transported greater distances. In Figure 5, a Nautilus Minerals schematic of the operational design (Gwyther, 2008a), the RALS output is labelled "Surface Plume from Return Water."

Equation 1 conceptually calculates the terminal settling velocity of a spherical particle.
w_t – terminal velocity: g – gravitational acceleration: ρ_s – mineral density: ρ_f – fluid density:

d – diameter: C_d *– drag coefficient.* Adapted from the Newtonian expression of drag resistance (Cheng, 1997)

$$w_t = \sqrt{\frac{4 \cdot g \cdot (\rho_s - \rho_f) \cdot d}{3 \cdot \rho_f \cdot C_d}} \quad \text{[Eq. 1]}$$

Equation 2 demonstrates the inequality of spherical and cubic volumes, $k = 0.5236$.

$$\frac{4}{3} \cdot \pi \cdot \left(\frac{d}{2}\right)^3 = k \cdot d^3 \quad \text{[Eq. 2]}$$

Equation 3 is a modification of Equation 1, k is included to better estimate velocity of cubic particles. C_d is assumed as 0.8, as for a cube (Engineering Toolbox, 2004).

$$w_t = \sqrt{\frac{4 \cdot g \cdot (\rho_s - \rho_f) \cdot d}{(3 \cdot k) \cdot \rho_f \cdot C_d}} \approx \sqrt{\frac{4 \cdot 9.81 \cdot (\rho_s - \rho_f) \cdot \mathbf{8{\times}10^{-6}}}{3 \cdot 0.5236 \cdot \rho_f \cdot \mathbf{0.8}}} = \sqrt{\frac{2.5{\times}10^{-4} \cdot (\rho_s - \rho_f)}{\rho_f}} \quad \text{[Eq. 3]}$$

ρ_f will be stated as 1035.37 kg m^{-3}, typical of seawater at 1.55 km depth, 0ºC and 35 Practical Salinity Units (PSU), an approximation for Solwara 1 (Encyclopædia Britannica, 2018)

The remaining variable is mineral density. Table 1 lists the typical sulphide minerals. Their density (g cm^{-3} (Korbel & Novák, 1999), scaled to kg m^{-3} for Equation 3) and settling velocity (w_t m s^{-1}) is presented assuming an 8µm grain diameter with a cubic, texturally immature, shape (C_d = 0.8), using Equation 3. Target metals are indicated as bold in formulae, as extracted from Korbel & Novák (1999).

Table 1: Mineral densities and settling velocities from return water, as for Solwara 1, 1.55km depth.

Mineral	***Formula***	ρ_s **(g cm^{-3})**	W_t **(m s^{-1}) [8µm]**	W_t **(m s^{-1}) [0.1µm]**
Quartz	SiO_2	*2.6*	*0.0194*	*0.0022*
Jalpaite	$\mathbf{Ag_3Cu}S_2$	*6.8*	*0.0373*	*0.0042*
Sphalerite	$\mathbf{Zn}S$	*4.1*	*0.0272*	*0.0030*
Chalcopyrite	$\mathbf{Cu}FeS_2$	*4.3*	*0.0281*	*0.0031*
Pyrrhotite	$Fe_{1-x}S$ *(x = 0-0.17)*	*4.7*	*0.0297*	*0.0033*
Millerite	NiS	*5.4*	*0.0325*	*0.0036*
Galena	PbS	*7.6*	*0.0398*	*0.0045*
Covelite	CuS	*4.6*	*0.0293*	*0.0033*
Calaverite	$\mathbf{Au}Te_2$	*9.3*	*0.0447*	*0.0050*
Pyrite	FeS_2	*5.0*	*0.0309*	*0.0035*
Marcasite	FeS_2	*4.9*	*0.0305*	*0.0034*

As Quartz has the lowest settling velocity in Table 1, it is used to calculate the maximum extent of the ACS plume.

ii. ACS Plume in Quiescent Water

This section assumes that there is no current velocity in any direction at or below the terminus of the return water outlet, that the flux of return water is constant, and the outlet water is of equal density to the uniform ambient water.

The output discharge is taken through two pipes, assuming both are half the RALS pumping rate, the outflow will be 2× 0.14 m^3 s^{-1}. To calculate the velocity of the return water, a cross-sectional area of the outlet is required. However, no specification or design is included in any found literature. In lieu of an absolute figure, an informed estimate must suffice: Figure 6, a photograph of segments of the RALS published by the manufacturer, illustrates a nominal scale of the equipment.

Figure 6 is analysed using the cross-section of the beam as a scale, which is assumed to be a

Figure 6: RALS segments manufactured for Nautilus Minerals Inc. (GMC Deep Water Ltd., 2016). The third segment is propped by a beam highlighted with a blue circle: the return water outlets are highlighted with red circles.

10cm × 10cm beam. Nominally, a 0.1 metre width is used for the beam. Visually, comparing the beam and outlets (red circles) an outlet radius of 0.02 metres is taken.

The total cross-sectional area, of the two return water outlets, is:

$2 \times (2\pi(0.02^2) = 5.0265 \times 10^{-3}$ [m^2]

The effective velocity at the return water outlet, assuming no resistance, is:

$$\frac{0.28\ [m^3\ s^{-1}]}{5.0265{\times}10^{-3}\ [m^2]} = 55.70\ [m\ s^{-1}]$$

To estimate the range of the ACS plume, this work adopts the inverse square law for a half sphere, as in Equation 4. *V_s - Velocity at displacement, s; V_0 – Velocity at source (55.7 m s^{-1}); s – displacement from source (m).*

$$V_s = \frac{V_0}{2\pi\ s^2} \qquad \text{[Eq. 4]}$$

Figure 7 is a computation of logarithmic speed dispersion, based on Equation 5. The colour map is designed to highlight where velocities are greater than that of the settling velocities of:

(orange) 8µm Quartz particles; (yellow) 0.1µm Quartz Particles; and (Blue-Grey), no relevant settling velocities, i.e. all particles settle.

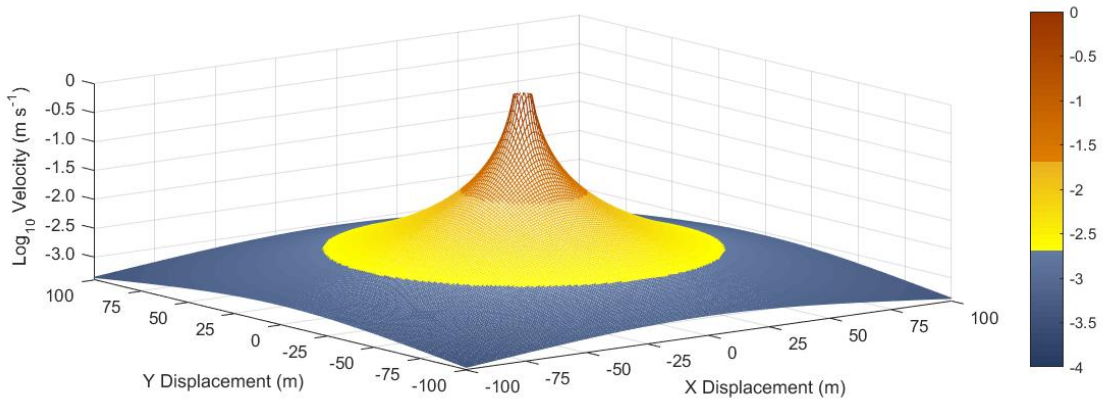

Figure 7: MATLAB computation of speed dispersion obeying inverse square law for a half sphere, initial velocity as 55.7 m s^{-1}. Colourmap indicates regions of suspension: orange (8µm); yellow (0.1µm); blue-grey (no suspension).

The settling velocity for 8µm quartz particles (0.0194 m s^{-1}) is achieved at 21.37m from the source, given circular distribution, this ACS is deposited over 2871.1 m^2.

The settling velocity for 0.1µm quartz particles (0.0022 m s^{-1}) is achieved at 63.47m from the source, given concentric circular distribution, this ACS is deposited over 25318.2 m^2.

iii. ACS Plume in Dynamic Water

This section discusses how natural currents may affect the distribution of the ACS plume: for ease of computation, these currents will act horizontally in one plane.

Quantitative data on natural deep-sea currents is sparsely found, although the consensus is that currents act on scales of hundreds to thousands of metres, with sluggish velocities. Figure 8 presents data extracted from Visbeck (2002), averaged from surveys in Hawaii and Tropical Atlantic. Deep water currents (at depths of ~1500m) are typically measured between 0.01 to 0.05 m s^{-1} (Visbeck, 2002; *e.g.* Vic, et al., 2018).

Similar values are seen in the locality of Solwara 1. The median bottom-water current velocity was recorded by Coffey Natural Systems (on consultancy for Nautilus) as 0.06 m s^{-1}, only 5% of the current speeds exceeded 0.15 m s^{-1}, with a maximum recording of 0.35 m s^{-1} (Gwyther, 2008a).

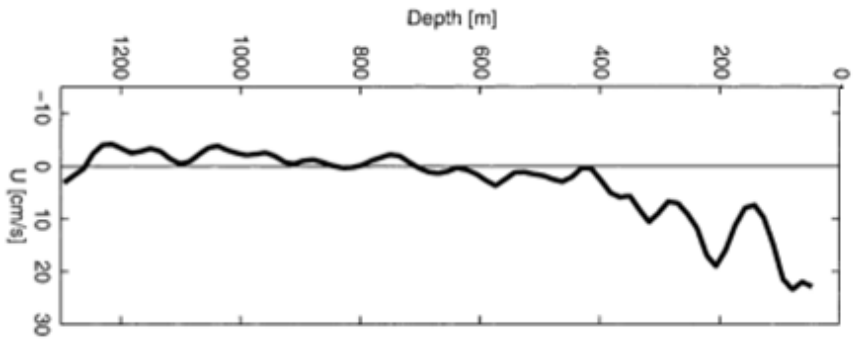

Figure 8: A typical Velocity-Depth profile extracted from Visbeck (2002), placing bottom currents as 0.01 to 0.10 m s^{-1}.

These velocities are indeed relevant for Solwara 1, and shallow hydrothermal deposits (~1500m), however, the MHDs are found at depths up to 5000m: surveys of deep and bottom currents around Challenger Deep and Mariana Trench include super-annual observations of mean current velocities in water depths in the region of 6000-7000m, data is presented in Table 2 (extracted and adapted from Taira, *et al.* (2004)).

Table 2: Super-Deep-water velocities, falling in the orders of magnitude of 10^{-3} to 10^{-2} m s^{-1}.

Record	Meter depth/Water depth	Days, and periods	East-component	North-component
CD11	6608/ 7034 m	443d, Jul 31 '95–Oct 15 '96	−0.77 ± 1.08 cm s^{-1}	0.27 ± 0.50 cm s^{-1}
CD12	7009/ 7034 m	443d, Jul 31 '95–Oct 15 '96	−0.60 ± 1.03 cm s^{-1}	−0.35 ± 0.56 cm s^{-1}
CD31	6214/ 6640 m	417d, Aug 26 '95–Oct 15 '96	0.09 ± 0.87 cm s^{-1}	0.19 ± 0.65 cm s^{-1}
CD32	6615/ 6640 m	441d, Aug 2 '95–Oct 15 '96	−0.48 ± 1.34 cm s^{-1}	−0.04 ± 1.03 cm s^{-1}

Based on these collations of data, the net velocities will be modelled under ambient current velocities rising incrementally from 10^{-3} m s^{-1} to the settling velocity of 8µm quartz particles. Figure 9 shows the labelled axis, without data, indicating the direction of ambient current velocity. Figure 10 is a set of MATLAB computations of logged net velocities under currents of; A) 0 m s^{-1}. B) 0.001 m s^{-1}. C) 0.002 m s^{-1}. D) 0.005 m s^{-1}. E) 0.010 m s^{-1} and F) 0.020 m s^{-1}.

Figure 9 and 10 z-axis limits are defined by minimum: the settling velocity of 0.1µm cubic quartz particles, 0.0022 m s^{-1} (Log -2.66); and maximum 1.0 m s^{-1} (Log 0).

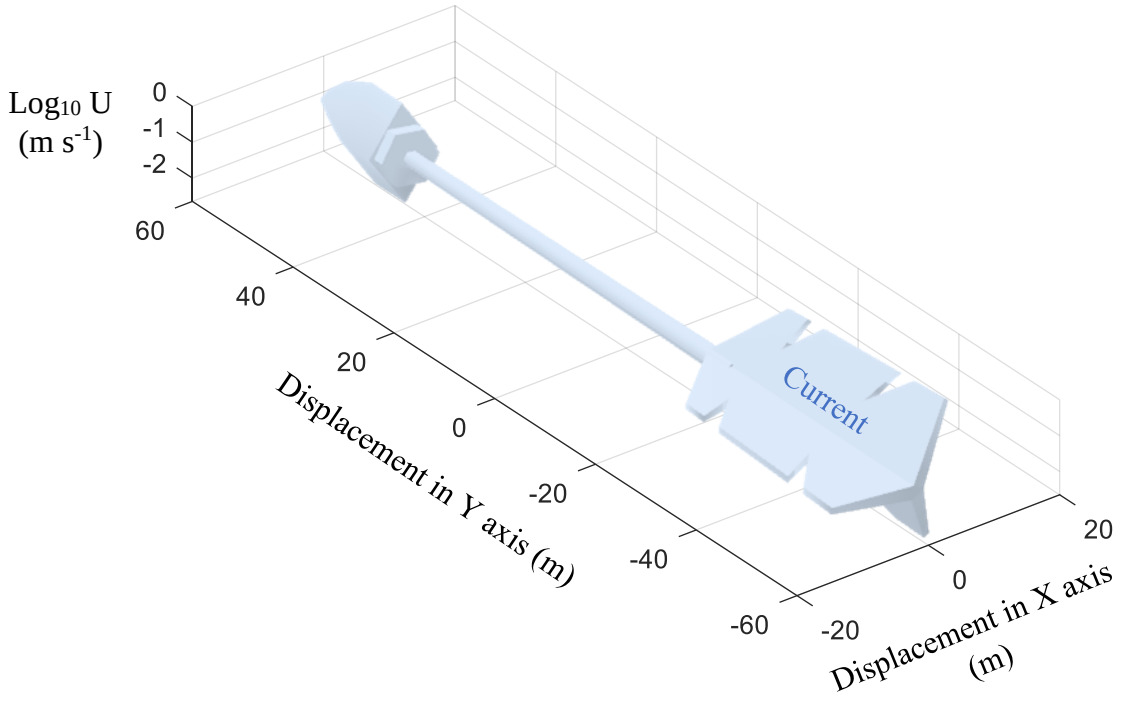

Figure 9: Schematic of MATLAB computation axis, with annotated current direction.

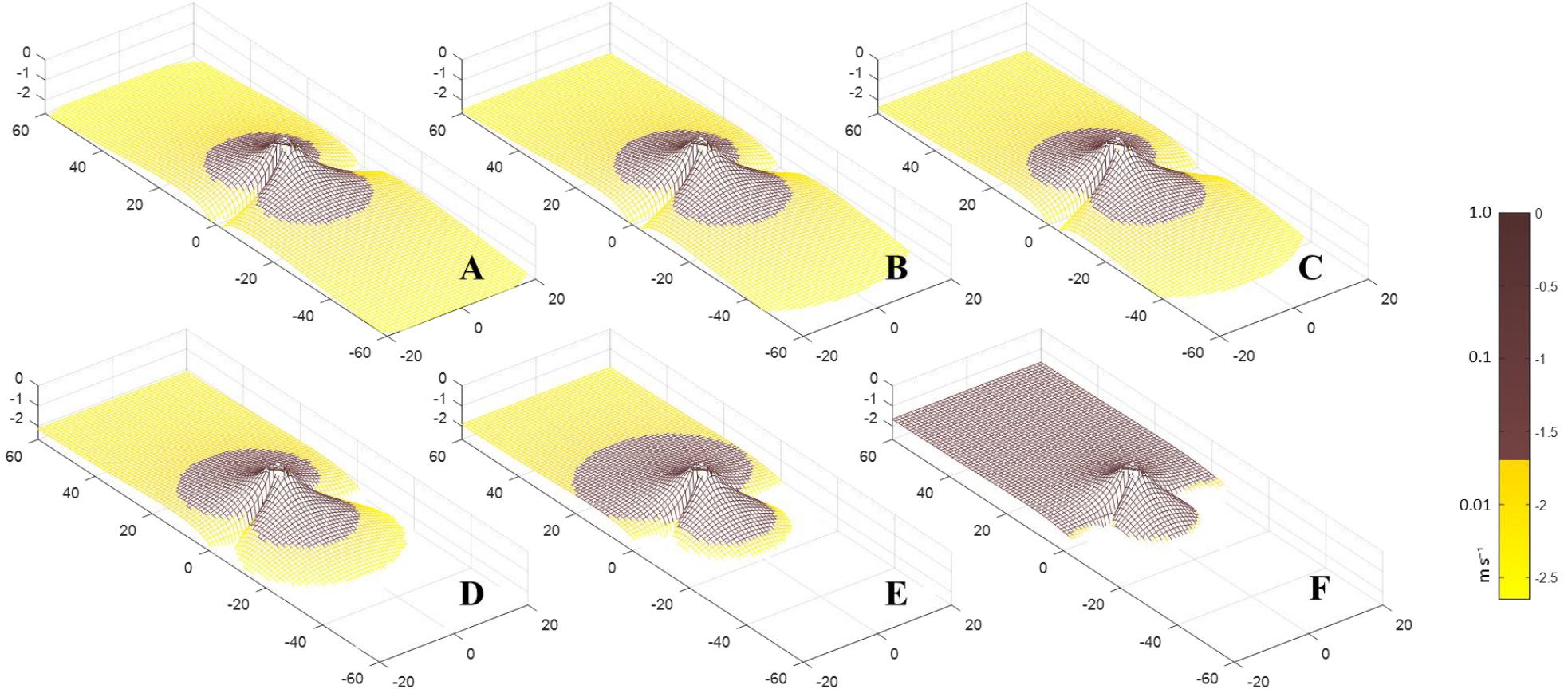

Figure 10: MATLAB computation of mono-axial velocity component of speed dispersion (as Figure 7, from Equation 5) in an ambient current field of: A) 0 m s^{-1}. B) 0.001 m s^{-1}. C) 0.002 m s^{-1}. D) 0.005 m s^{-1}. E) 0.010 m s^{-1}. F) W_s of 8µm cubic quartz particles (modelled as 0.020 m s^{-1}). Colourmap: (Brown) velocities >W_s of 8µm cubic quartz particles [0.0194 m s^{-1}]. (Yellow) velocities >Ws of 0.1µm cubic quartz particles [0.0022 m s^{-1}].

Figure 10 demonstrates that in an increasing current velocity field, the 'head' of the plume (where y<0) decreases in extent, while the tail of the plume (y>0) increases in extent until the particle settling velocity is achieved, and the extent is effectively infinite unless conditions change. This can be hydrodynamic or sediment characteristics.

iv. Hydrodynamics for Computing ACS Plumes

These computations do not include the variability of current velocity, unfortunately this data is very scarce. Long-term studies indicate a great range of variability. Figure 11, is a graph showing seabed current velocity data in the Gulf of California, at depths of ~4120m: this data has been digitised from *Figure 1* in Aleynik, *et al.* (2017) and the square root taken to represent a scalar speed (m s^{-1}).

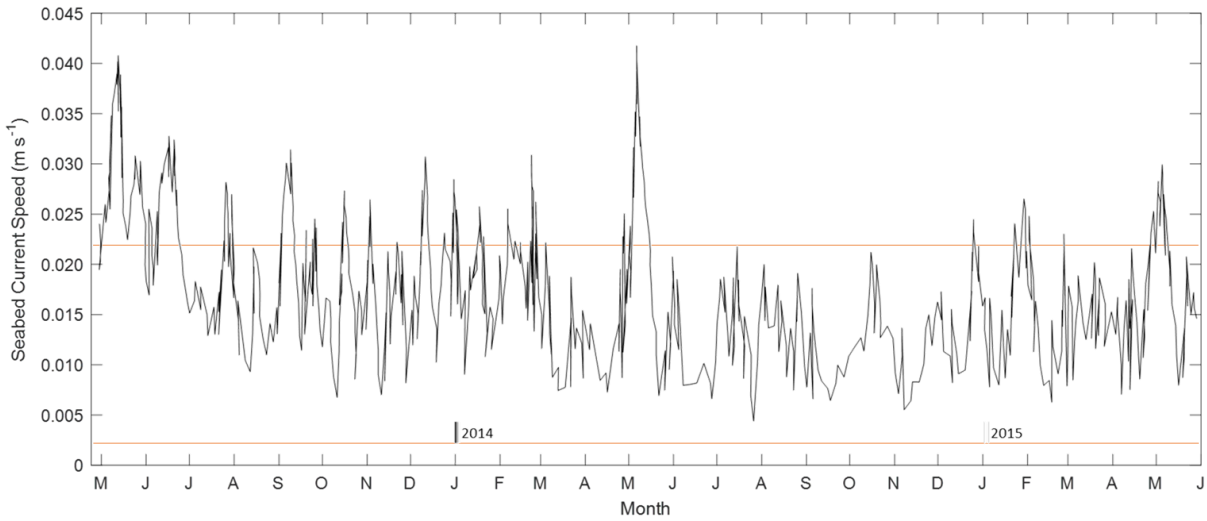

Figure 11: Seabed Current Speeds (m s^{-1}) over 25 months on the abyssal plains of the Gulf of California: data extracted and adapted from Aleynik, et al. *(2017). Orange line indicates settling velocities used since Section C) ii.*

Figure 11 illustrates two key points, the first is spatial variation in deep current speeds: the Gulf of California speeds are an order of magnitude greater than those previously discussed in the challenger deep. Although, the Gulf of California is prospected for a different marine mineral resource.

The second is the cyclicity of velocity variation: to discuss this further, this data has been analysed in MATLAB using the Fast Fourier Transform (FFT) algorithm: to resolve the magnitude of frequencies (oscillations per day) observed in this data. Figure 12 presents this Fourier Transform plot on logarithmic axis, annotations indicate: A) Sub-Decadal cycles, *e.g.* El Niño-Southern Oscillation [taken as an upper average of seven years] (NOAA Climate.gov Staff, 2016); B) Annual variation; C) Seasonal Variation; D) The Spring-Neap Cycle.

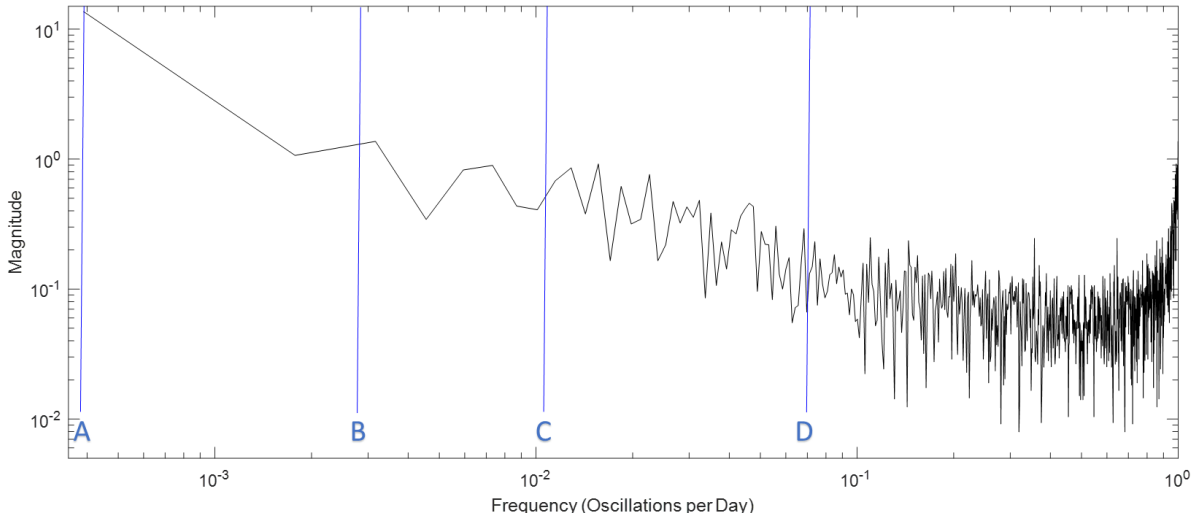

Figure 12: Fourier Transform Spectra of Figure 11 data. Computed using MATLAB. A negative trend is observed between magnitude and frequency.

The Fourier Transform Spectra illustrates that the strongest signals in deep water current velocity variations are long-term climatic cycles: followed by annual variability, and noise (high frequency). It may be suggested that seasonal variation could have a greater effect at higher latitudes.

Critically, long-term oceanographic study is required to accurately predict ACS plumes and ACS dispersion: where currently, the data is spatially inadequate.

The Solwara 1 site underwent a twelve-month physical oceanography survey, although no sign of Fourier analysis has been presented. Therefore, if an understanding of the regions' long-term cyclicity is absent, is that understanding also temporally inadequate?

v. Oxidative Dissolution of ACS

A change in sediment characteristics is achievable due to chemical reactions between ACS and ambient seawater.

The potential environmental impact of ACS is not limited to the physical smothering of the seabed environment: which is a common discussion topic in the case of nodule mining (*e.g.* Aleynik, et al., 2017).

In situ, MHDs are oxidised on the surface of the deposit: this process creates 'Gossans', which exhibit chemistry alike that to supergenic sulphide zone in terrestrial deposits (Atapour & Aftabi, 2007). Pyrite (FeS_2) will oxidise (Korbel & Novák, 1999). This process involves the oxidative dissolution of Pyrite, as simplified by Equation 5 from McKibben & Barnes (1986):

$$2\,FeS_2 + 7\,O_2 + 2\,H_2O \rightarrow Fe^{2+} + 2SO_4^{2-} + 2H^+ \qquad \text{[Eq. 5]}$$

The formation of the H^+ ions gives rise to local acidification, the same processes give marine hydrothermal plumes their characteristic low pH values; and underpin the environmental concerns in terrestrial mining due to "Acid Mine Drainage" (Johnson & Hallberg, 2005).

The following three statements discuss the *operandi* of oxidative dissolution reactions, and are then considered to act on the deposit and sulphide-rich ACS:

"Rates [of oxidative dissolution] are affected by temperature, pH, salinity, oxidising agents and their concentration, flow rate, grain size, surface area, pressure and impurities." (Fallon, et al., 2017)

"Reactive surface area is substantially different than total surface area. Oxidation is centred on sites of high excess surface energy such as grain edges and corners, defects, solid and fluid inclusion pits, cleavages, and fractures." (McKibben & Barnes, 1986)

"[A] reason for lower rates could be related to the build-up of ferric-oxide coating that would be enhanced at the higher oxidation rates and would inhibit oxygen availability at the pyrite surface." (Nicholson, et al., 1988)

The classic model of inorganic chemical reactions, 'collision theory' was put forward by Trautz (1916): this is used to compare the deposit and its constituent ACS.

The *in-situ* deposit, of mass *m*, can be thought to be a single massive cubic particle protruding from the seabed: five interfaces are thus in contact with ambient oxidising conditions, therefore only five of the six interfaces are susceptible to reaction (collision). There is the potential for sites of excess surface energy, more so in the form of defects and fractures. Critically, this large particle has comparatively very low surface area. Once the outer surface is oxidised, oxygen availability is inhibited to the remainder of the sulphide minerals.

This is illustrated in Figure 13, where dark blue particles are oxidised, medium blue particles

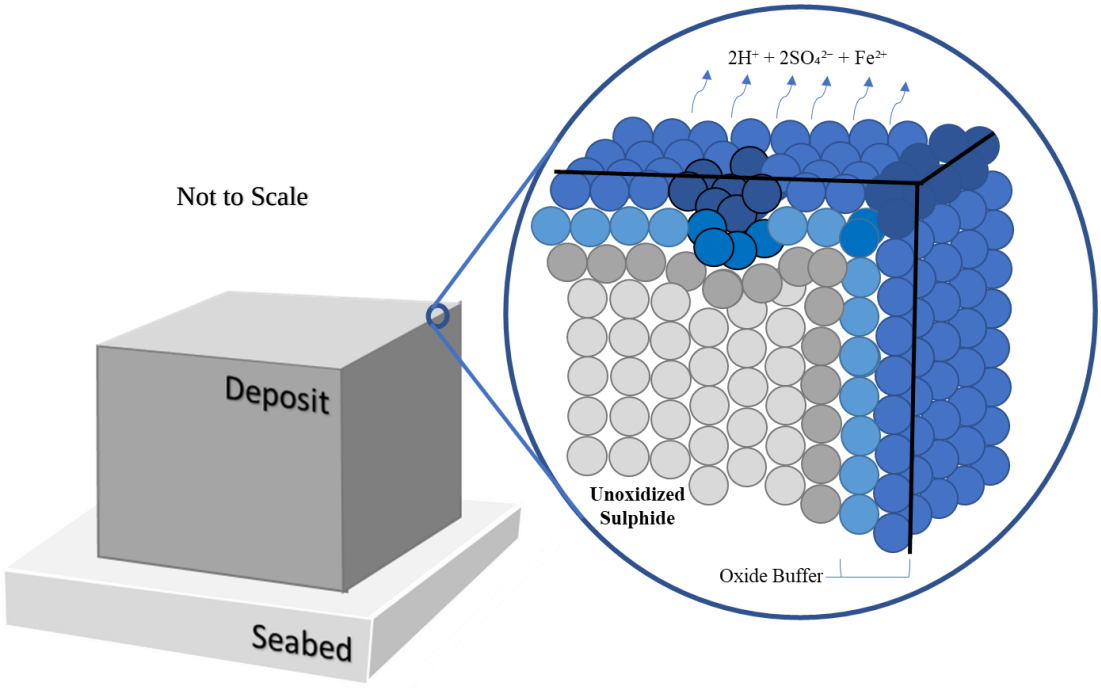

Figure 13: Surface oxidation and dissolution of an in-situ deposit indicating high surface excess energy.

are oxidising, dark grey particles will form the new sulphide interface, light grey particles will remain unoxidized. High excess surface energy is shown at the corner of the deposit and in surface imperfections for guidance.

The operational design for Solwara 1 includes a 100μm filter to avoid damage to the pumping system (Gwyther, 2008b), thus this work assumes 100μm as nominally the D_{95} grain size of sulphide grains. It is expected <5% of particles will be <8 μm (Gwyther, 2008a), so 8 μm is assumed as the D_5 grain size. Assuming normal distribution, the average (D_{50}) must fall half way, at 54 μm.

If the deposit [as Section C) v.] is 1 m^3, and 5 of 6 interfaces are reactive the active surface area must be 5 m^2. Disaggregate the deposit into 18518×18518×18518 54μm cubes (~1 m^3), and this surface area increases to:

$18518^3 \times 6 \times (54 \times 10^{-6}\ [m])^2 = 111101.8\ m^2$

Given the tendency for minerals to fail on planes of cleavage, existing fractures or defects, as per their definitions (Korbel & Novák, 1999), and that these sites are associated with 'high excess surface energy' (McKibben & Barnes, 1986), the results of the study presented above suggests the rate of reaction to increase disproportionatley more than the increase in total surface area.

As for the oxide coating, which inhibits the subsequent reaction, the proportion of the entire deposit being oxidised, and thus products of oxidation will increase. Also, particles which undergo secondary mineralisation may have significantly adjusted densities: potentially nullifying settling velocity considerations.

In terrestrial deposits, the enrichment of Chalcopyrite forms the secondary minerals: Chalcocite, Covellitte and Bornite. Oxidation forms Native Copper, Azurite, Malachite and Cuprite. The oxidation of Pyrite results in Limonite (Asmus, 2013). The formulae and densities of these secondary minerals, extracted from Asmus (2013) and Korbel & Novák, (1999) respectively, are presented in Table 3.

Table 3: Densities and formulae of sulphide, enriched secondary and oxidised secondary minerals. Data extracted from Asmus (2013) and Korbel & Novák (1999).

Mineral	Formula (Asmus, 2013)	ρ_s (g cm^{-3}) (*Korbel & Novák, 1999)
Chalcopyrite	$CuFeS_2$	*4.3*
Pyrite	FeS_2	*5.0*
Chalcocite	Cu_2S	*5.8*
Covellite	CuS	*4.6*
Bornite	Cu_5FeS_4	*5.1*
Azurite	$Cu_3(CO_3)_2(OH)_2$	*3.8*
Malachite	$Cu_2(CO_3)(OH)_2$	*4.1*
Cuprite	Cu_2O	*6.0*
Native Copper	Cu	*8.9*
Limonite (as Goethite)	$*Fe^{3+}O(OH)$	*4.3*

It is apparent, except for Goethite, that enriched and oxidised minerals have a greater settling velocity, thus need stronger currents to maintain suspension. This will be discussed further in later sections.

Discussion [D]

i. Interpreting "Environmental Impact"

This work has approached the term "Environmental Impact" objectively, however assessing impact is inherently subjective:

"Determining the significance of environmental impacts may be viewed as highly subjective judgment because it has to ruminate over the scientific facts (environmental, ecological and socioeconomic impacts) and subjective values (judgment, preference, value and concern)" (Liu, 2009)

The ecological implications of marine mining are unknown, some species have been identified, although "if you shine a light at an organism which has never seen light before…" (T. Sunde, Poseidon Offshore Mining: personal communication. March 13th, 2018)

The profound uncertainty around ecological impacts massively affects these subjective values. Even studying the abiotic environment, questions remain without answers.

Therefore, this work proposes concluding a Potential Impact Range (PIR) and Potential Impact Intensity (PII) abiotically.

For a comprehensive understanding of environmental impacts, a temporal scale must be defined. Take Solwara 1, Gwyther (2008b) states "It is expected to take three months to complete mining activities within [the Far-West Zone]. It is envisaged that mining of Central and West zones will take between 12 and 24 months, depending on conditions encountered. The final zones mined will be East Zone and Far East." Consider, nominally, a marine mine lifespan of three years. A user-defined Potential Impact Timeframe (PIT), summarising how long implications may arise after, may provide a more complete evaluation.

Subsequent study can then utilise the PIR, PII and PIT in evaluating the Environmental Impact at empirical locations.

ii. Environmental Impact of ACS Plume Deposition

This section deals with environmental impacts associated with the ACS Plume falling from suspension.

- PIR -

In quiescent conditions, this work considers the maximum extent of the ACS plume as that of 0.1μm quartz. Given some particle inertia, the region of deposition of grains will be a 2D torus (doughnut) shaped, at the termination of the plume. The deposition point (terminal torus diameter) for each mineral (as Table 1 and Table 3) is defined for quiescent water in Table 4.

The analysis in this work suggests that as ambient current velocity tends toward the settling velocity of a particle, its distribution becomes more "egg-shaped" (*i.e.* an asymmetrical oval)

with a tight “head” facing the flow and an elongated “tail” with the current direction. Ambient current velocities are shown in Figure 11 to quasi-frequently be greater, by variable magnitude, than the settling velocities of larger particles. The smallest of fractions settling velocity may be consistently surpassed and remain in suspension as trace products.

Table 4: Deposition point of each discussed mineral from return water: primary and secondary mineral separated by dotted line.

Mineral	W_t (m s^{-1}) [8µm]	Deposition Point (m) [8µm]	W_t (m s^{-1}) [0.1µm]	Deposition Point (m) [0.1µm]
Quartz	*0.0194*	*21.38*	*0.0022*	*63.48*
Jalpaite	*0.0373*	*15.42*	*0.0042*	*45.94*
Sphalerite	*0.0272*	*18.05*	*0.0030*	*54.36*
Chalcopyrite	*0.0281*	*17.76*	*0.0031*	*53.48*
Pyrrhotite	*0.0297*	*17.28*	*0.0033*	*51.83*
Millerite	*0.0325*	*16.52*	*0.0036*	*49.62*
Galena	*0.0398*	*14.92*	*0.0045*	*44.38*
Covelite	*0.0293*	*17.39*	*0.0033*	*51.83*
Callaverite	*0.0447*	*14.08*	*0.0050*	*42.11*
Pyrite	*0.0309*	*16.94*	*0.0035*	*50.33*
Marcasite	*0.0305*	*17.05*	*0.0034*	*51.06*
Chalcocite	*0.0339*	*16.17*	*0.0038*	*48.30*
Covellite	*0.0293*	*17.39*	*0.0033*	*51.83*
Bornite	*0.0313*	*16.83*	*0.0035*	*50.33*
Azurite	*0.0258*	*18.54*	*0.0029*	*55.29*
Malachite	*0.0271*	*18.09*	*0.0030*	*54.36*
Cuprite	*0.0346*	*16.01*	*0.0039*	*47.68*
Native Copper	*0.0436*	*14.26*	*0.0049*	*42.53*
Limonite (as Goethite)	*0.0281*	*17.76*	*0.0031*	*53.48*

Table 4 can be taken as the initial deposition range of sediments. Plume and deposit reworking will be achieved under intervals of increased current velocities. Means of predicting these intervals (like that of Fourier analysis) would allow the estimation of Potential Impact Range across Potential Impact Timeframes, this would enable management of the environmental impact.

- PII -

The Potential Impact Intensity of ACS deposition on the seabed is challenging to predict, as it is dependent on the proportion of minerals in the plume. The minerals discussed exhibit some variability in “deposition point.”

Figure 14 is a simple histogram counting the number of discussed minerals, of bimodal particle size (8µm and 0.1µm). The process of exploitation will produce a range of different particle sizes. This proportionality is also a challenge to predict, however it is observed that the spatial distribution of larger particles is tighter than that of finer particles. Following this assessment logically, as particle size decreases: the median distance increases and the range of distances increases. The sum of each ‘mode’ (particle size) will produce a distribution of strong positive skew. Thus, the maximum intensity of ACS deposition will manifest at approximately 18-20 metres from the source in quiescent water. The minimum distance from

the source is 14.08 metres, the maximum extent is 63.48 in quiescent water. Dynamic conditions will decrease intensity but increase range and extent.

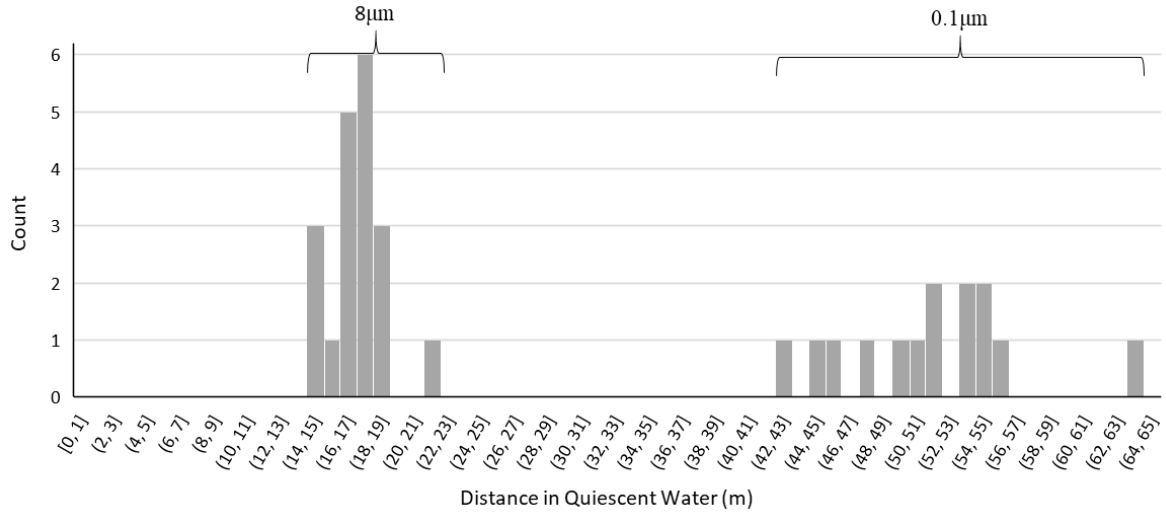

Figure 14: Histogram of distribution of bimodal ACS minerals in quiescent water.

- PIT –

The Potential Impact Timeframe of ACS deposition is relevant for dynamic conditions. For which an understanding of the cyclicity of these conditions is required. *How could this be done?*

As this work has presented, using an FFT algorithm on adequate-tide-spatial-resolution data of deep water velocities will present the relative magnitude of cycles in that location (varying with all three axes). By cutting out "noise", in Figure 11 taken as $>10^{-1}$ Oscillations per Day and running an Inverse Fast Fourier Transform (IFFT), a simplified polynomial model of velocity variability is defined.

From this model: define a settling velocity; integrate the sum of the model minus the settling velocity. In defining the Potential Impact Timeframe, T, as an upper bound, the PIR of nominal particle sizes can be calculated (within the PIT) by taking the integral of that sum.

This work will run through this processes' outputs and include MATLAB code in the appendix of this work:

For raw signal, see Figure 11.

For FFT of the signal, see Figure 12.

Discard FFT data where Frequency is greater than 10^{-1} oscillations per day. This may vary by signal and is subject to analysis. Run an IFFT algorithm on the remaining frequencies and plot with respect to time.

Note: at the periphery of known x-axis data, the y-data increases to extremes, these points can be discarded.

The resulting graph for analysis of Aleynik *et. al.* (2017) data is presented in Figure 15.

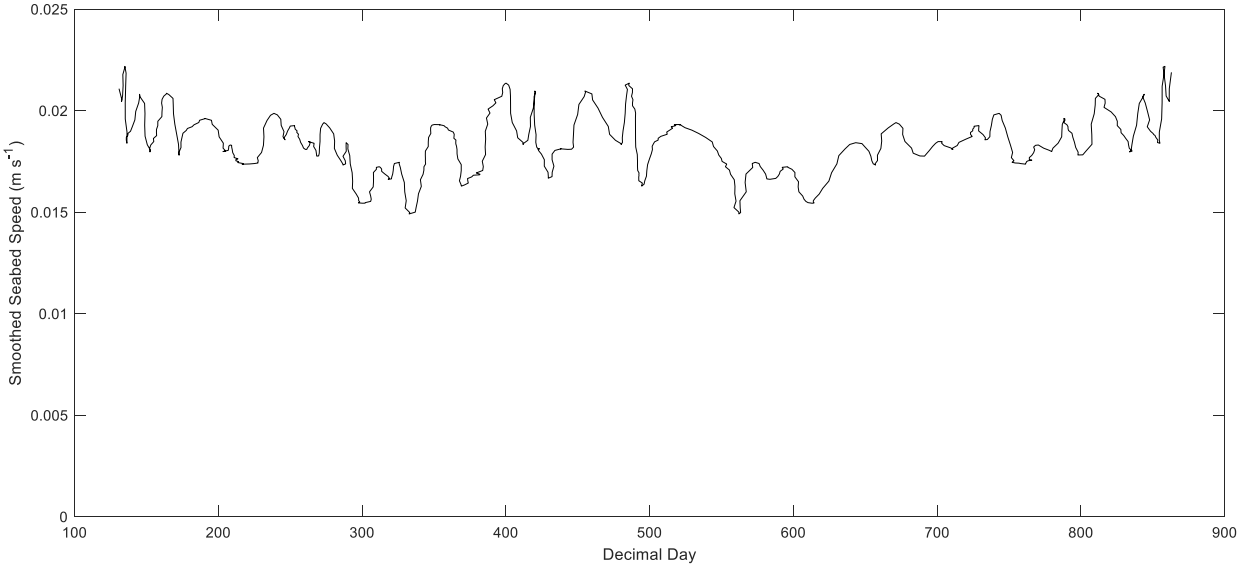

Figure 15: Seabed Current Speed model after Inverse Fast Fourier Transform (IFFT)

Deducting a settling velocity, for example that of 8μm quartz particles, will produce a graph potentially crossing y=0 m s^{-1}. By redefining negative values as 0, the sediment transport speed profile by decimal day is obtained, as in Figure 16.

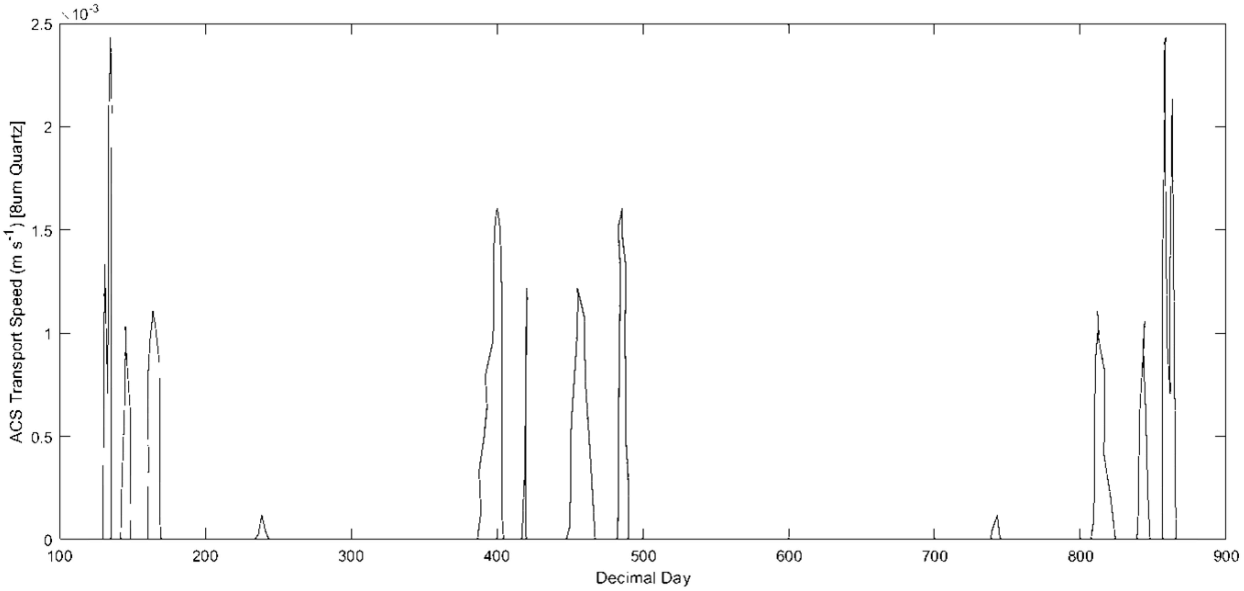

Figure 3: ACS Transport speeds for 8μm Quartz Particles

Integration in MATLAB is possible using the CUMTRAPZ (Cumulative Trapeze) function, the resulting plot is displayed in Figure 17.

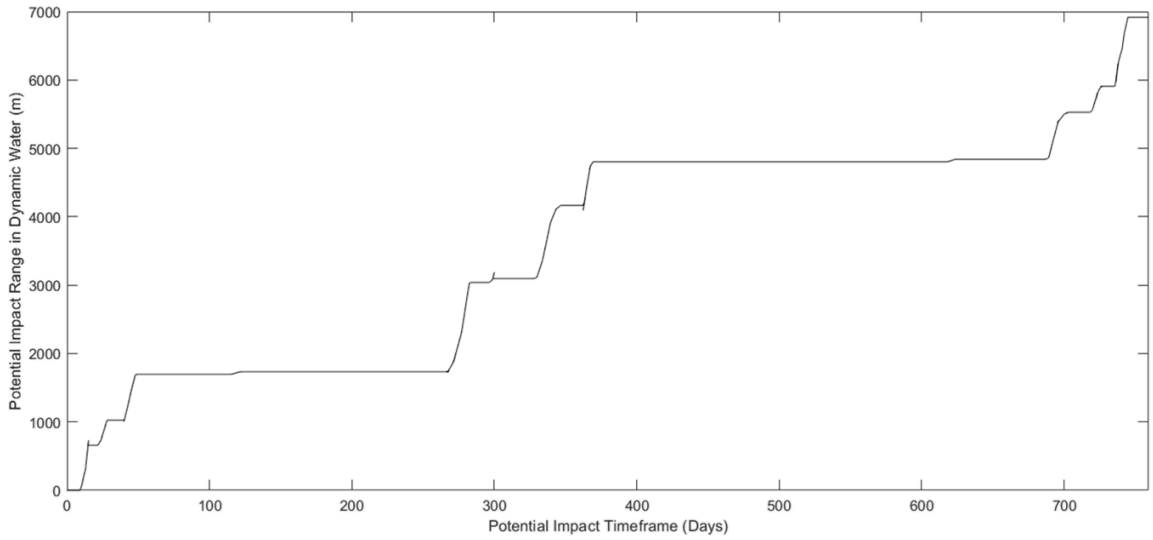

Figure 17: Potential Impact Range in given Potential Impact Timeframe for 8μm Quartz.

Included in the appendix is code including user-defined physical ACS properties, and a space to upload seabed velocity current data. The code will calculate the PIR in dynamic water of each iteration, plot a histogram of relative Potential Impact Intensity, given a user-defined Potential Impact Timeframe.

iii. Environmental Impact of Oxidative Dissolution

This section focusses on the effect of acidification, toxin enrichment and nutrient enrichment of ambient water due to the oxidative dissolution of ACS plumes.

- PIR -

The deep ocean is characteristically a low energy environment, but it has a weak density gradient (Aleynik, et al., 2017), therefore small chemical changes can have wide, even regional, implications in the water column.

- PII -

The intensity, or measure, of acidification at such depth will be challenging to calculate or obtain: although it must be noted this acts on the entirety of the deposit ACS, not only the fraction in return water.

Conclusions **[E]**

i. Evaluating Aims and Findings

This work has identified two potential environmental impacts associated with Anthropogenically Created Sediment (ACS) formed when exploiting Marine Hydrothermal Deposits (MHDs).

Introducing the functions; Potential Impact Range (PIR), Potential Impact Intensity (PII), within a user-defined Potential Impact Timeframe (PIT) has allowed the objective evaluation of environmental impact from exploiting MHDs to be conducted. The procedure is given in the appendix.

The aims are accomplished for the quantifying the environmental impact of ACS plumes, despite a lack of available data: the product of this work may be used as a tool to quantify the functions, after the collection of data for new projects.

However, quantification of environmental impacts produced by oxidative dissolution is not achieved.

Among the findings of this work, criticism falls of the lack of information presented on how data has been processed in existing Environmental Impact Assessments.

ii. Recommendations for Future Study

The products of oxidative dissolution will be at an increased level due to the methods of exploiting MHDs. These will likely constitute the widest implicating environmental impact, as they will be dispersed in solution.

Study on energy and pycnocline (density gradient) strength variation, both spatial and temporal, in deep water environments (>1500m) would provide a basis of data for dispersion modelling. A strong model could be used to identify areas where the environmental impact, PIR or PII, is disproportionately increased. Identification of such areas will benefit efforts to manage the environmental impact posed by marine mining.

iii. Final Remarks

The Solwara 1 project is ‘anticipated to commence in late 2019’ (Naultilus Minerals Inc., 2018), these first operations will be ground breaking. Marine Mining is a phenomenal advancement for the mining industry, but it is a venture into a poorly understood abyss. The absence of data may prove to have devastating consequences which ultimately may not even be realised, given the remote and inhospitable environment.

Thus, the scientific community must not follow the mining industry. It must lead.

In the “race for second place” for commodity (T. Sunde, Poseidon Offshore Mining: personal communication. March 13th, 2018), objectivity is a necessity.

***References* [F]**

Aleynik, D., Inall, M. E., Dale, A. & Vink, A., 2017. Impact of remotely generated eddies on plume dispersion at abyssal mining sites in the Pacifc. *Scientific Reports,* 7(1), p. Online.

Andres, C., 2013. *World's top 10 gold deposits.* [Online]
Available at: http://www.mining.com/web/worlds-top-10-gold-deposits/
[Accessed 1 February 2018].

Asmus, B., 2013. *Gossan or the iron cap.* [Online]
Available at: http://en.archaeometallurgie.de/gossan-iron-cap/
[Accessed 22 March 2018].

Atapour, H. & Aftabi, A., 2007. The Geochemistry of gossans associated with Sarchemshmeh porphyry copper deposit, Rafsanjan, Kerman, Iran: Implications for exploration and the environment. *Journal of Geochemical Exploration,* 93(1), pp. 47-65.

Brown, A. & Hauton, C., 2018. Ecotoxicological responses to chalcopyrite exposure in a proxy for deep-sea hydrothermal vent shrimp: implications for seafloor massive sulphide mining. *Chemistry and Ecology*, 34(4), pp. 391-396.

Camborne School of Mines, 2013. *"if it cannot be grown, it has to be mined",* Exeter: University of Exeter.

Cheng, N.-S., 1997. Simplified settling velocity formula for sediment particle.. *Journal of Hydraulic Engineering*, 123(2), pp. 149-152.

Department of Economic and Social Affairs: Population Division, 2017. *World Population Prospects: The 2017 Revision,* New York: United Nations.

Desjardens, J., 2016. *The Extraordinary Raw Materials in an iPhone 6s.* [Online]
Available at: www.visualcapitalist.com/extraordinary-raw-materials-iphone-6s/
[Accessed 26 January 2018].

Encyclopædia Britannica, 2018. *Density of seawater and pressure.* [Online]
Available at: https://www.britannica.com/science/seawater/Density-of-seawater-and-pressure
[Accessed 1 March 2018].

Engineering Toolbox, 2004. *Drag Coefficient.* [Online]
Available at: https://www.engineeringtoolbox.com/drag-coefficient-d_627.html
[Accessed 1 March 2018].

Fallon, E. K., Petersen, S., Brooker, P. A. & Scott, T. B., 2017. Oxidative dissolution of hydrothermal mixed-sulphide ore: An assessment of current knowledge in relation to seafloor massive sulphide mining. *Ore Geology Reviews,* Volume 86, pp. 309-377.

Freeport McMoRan, 2016. *Driven By Value: 2016 Annual Report,* Phoenix, Arizona: Freeport McMoRan.

GMC Deep Water Ltd., 2016. *GMC Delivers Riser and Lifting System (RALS) for Seafloor Mining Project.* [Online]
Available at: http://gmcdeepwater.com/gmc-delivers-riser-and-lifting-system-for-seafloor-mining-project/
[Accessed 11 March 2018].

Gwyther, D., 2008a. *Environmental Impact Summary: Solwara 1 Project: Executive Summary,* Brisbane: Coffey Natural Systems.

Gwyther, D., 2008b. *Environmental Impact Statement: Solwara 1 Project: Main Report,* Brisbane: Coffey Natural Systems.

Haxel, G. B., Hendrick, J. B. & Orris, G. J., 2002. *Rare Earth Elements—Critical Resources for High Technology,* s.l.: USGS.

Hoagland, P. et al., 2010. Deep-sea mining of seafloor massive sulphides. *Marine Policy,* Volume 34, pp. 728-732.

ICSG, 2017. *The World Copper Factbook 2017,* Lisbon: International Copper Study Group.

Jeswiet, J., 2017. Including Towards Sustainable Mining in evaluating mining impacts. *Procedia CIRP,* 62(Open Access), pp. 494-499.

Johnson, D. B. & Hallberg, K. B., 2005. Acid mine drainage remediation options: a review. *Science of the Total Environment,* Volume 338, pp. 3-14.

Korbel, P. & Novák, M., 1999. *The Complete Encyclopedia of Minerals.* s.l.:Rebo International.

Liu, K., 2009. A Qualitative Decision Support for Environmental Impact Assessment Using Fuzzy Logic. *Journal of Environmental Informatics,* 13(2), pp. 93-103.

Lowe, J., 2012. *Solwara Project Resource Estimate,* Queensland: Golder Associates.

McKibben, M. A. & Barnes, H. L., 1986. Oxidation of pyrite in low temperature acidic solutions: Rate laws and surface textures. *Geochimica et Cosmochimica Acta,* 50(7), pp. 1509-1520.

Naultilus Minerals Inc., 2018. *Nautilus Minerals Seafloor Production Vessel Launched,* Toronto: Naultilus Minerals Inc..

Nautilus Minerals Niugini, 2008. *Sources of potential impact form offshore mining operations,* Brisbane: Coffey Natural Systems.

Nicholson, R. V., Gillham, R. W. & Reardon, E. J., 1988. Pyrite oxidation in carbonate-buffered solution: 1. Experimental kinetics. *Geochimica et Cosmochimica Acta,* 52(5), pp. 1077-1085.

NOAA Climate.gov Staff, 2016. *El Niño and La Niña: Frequently asked questions.* [Online]
Available at: https://www.climate.gov/news-features/understanding-climate/el-ni%C3%B1o-and-la-ni%C3%B1a-frequently-asked-questions
[Accessed 15 March 2018].

Pryce, W., 1778. Introduction. In: *Mineralogia Cornubiensis; a Treatise on Minerals, Mines and Mining.* London: Phillips, pp. 30-59.

Szamalek, K., Marcionwska, A., Nejbert, K. & Speczik, S., 2011. Sea-floor massive sulphides from the Galápagos Rift Zone – mineralogy, geochemistry and economic importance. *Geological Quarterly*, 55(3), pp. 187-202.

Taira, K., Kitigawa, S., Yamashiro, T. & Yanagimoto, D., 2004. Deep and Bottom Currents in the Challenger Deep, Mariana Trench, Measured with Super-Deep Current Meters. *Journal of Oceanography,* 60(6), pp. 919-926.

Trautz, M., 1916. Das Gesetz der Reaktionsgeschwindigkeit und der Gleichgewichte in Gasen. Bestätigung der Additivität von Cv-3/2R. Neue Bestimmung der Integrationskonstanten und der Molekül durchmesser. *Zeitschrift fúr anorganische und allgemeine Chemie (Journal of Inorganic and General Chemistry),* 96(1), pp. 1-28.

Van Wijk, J. M., 2016. *Vertical hydraulic transport for deep sea mining: A study into flow assurance,* s.l.: TU Delft Library.

Vic, C., Gula, J., Roullet, G. & Pradillon, F., 2018. Dispersion of deep-sea hydrothermal vent effluents and larvae by. *Deep Sea Research Part I,* In Press(In Press), p. In Press.

Visbeck, M., 2002. Deep Velocity Profiling Using Lowered Acoustic Doppler Current Profilers:. *JOURNAL OF ATMOSPHERIC AND OCEANIC TECHNOLOGY.*

Wentworth, C. K., 1922. A Scale of Grade and Class Terms for Clastic Sediments. *The Journal of Geology,* pp. 377-392.

Appendix [G]

This script is submitted as supplement material for the Dissertation, *"The Environmental Impact of Marine Mining"*, which aimed to quantify the Potential Impact Range (PIR), and Potential Impact Intensity (PII) within a user-defined Potential Impact Timeframe (PIT) for sediment plumes formed by the exploitation of Marine Hydrothermal Deposits.

Script

```
clc;close all;clear all
```

Constants and Assumptions for Settling Velocity

```
g = 9.81; %*Acceleration due to Gravity* m s^-^2
rhoF = 1035; %*Fluid Density* kg m^-^3.
Cd = 0.8; % Drag Coefficeint of a cube
k = 0.5236; % Modification constant, see Equation 2.
```

Modelling Velocity Dispersion in Quiescent Water

```
q = 0.28; % *OUTLET FLUX* m^3 s^-^1
n = 2; % Number of return outlets
r = 0.02; % *RADIUS* m
area = pi*n*2*(r^2); % *TOTAL OUTLET CROSS SECTION AREA* m^2
V0 = q/area; % *INITIAL VELOCITY*
```

User Defined Variables - Mineral 1

```
rho1 = 2650; %*DENSITY*: As for Quartz, in iterations input mineral density in kg m^-^3.
a1 = 1; %*RELATIVE MINERAL ABUNDANCE* If known, input the relativ abunance to Quartz in
iterations.
d1 = 0.000008; %*PARTICLE SIZE* m. 0.000001 < d1 < 0.00008
A1 = 1; %*RELATIVE PARTICLE SIZE* If known, input the relativ abunance to 0.00008 in
iterations.
w1 = ((4*g*(rho1-rhoF)*d1)/(3*k*Cd*rhoF))^0.5; %m s^-^1
PIR_1 = (V0/(2*pi*w1))^0.5;
```

User Defined Variables - Mineral 2

```
rho2 = 5000; %*DENSITY*: As for Pyrite,kg m^-^3.
a2 = 7; %*RELATIVE MINERAL ABUNDANCE* Example.
d2 = 0.000008; %*PARTICLE SIZE* m. 0.000001 < d1 < 0.00008
A2 = 0.4; %*RELATIVE PARTICLE SIZE* Example.
w2 = ((4*g*(rho2-rhoF)*d2)/(3*k*Cd*rhoF))^0.5; %m s^-^1
PIR_2 = (V0/(2*pi*w2))^0.5;
```

User Defined Variables - Mineral *N*

Copy and paste "User Defined Variables - Mineral 1", substituting the number of iteration, N, in place of '1'.

rhoN =

aN =

dN =

AN =
wN = ((4*g*([rhoN]-rhoF)*[dN])/(3*k*Cd*rhoF))^0.5
PIR_N = (V0/(2*pi*[wN]))^0.5

Potential Impact Intensity in Quiescent water

PII is given as a relative intensity and is unitless.

```
m1 = a1*A1; % Abundance Product relative to Quartz (1).
m2 = a2*A2; % Abundance Product relative to Quartz (a=7, A=0.4)
figure % Open figure window
x=[PIR_1,PIR_2]; % Continue, x=[PIR_1,PIR_2, ...PIR_N]
y=[m1,m2]; % Continue, x=[m1,m2, ...mN]
scatter(x,y,'k');
xlim ([0 75]);
ylim ([0 10]);
xlabel('Distance from Outlet (m)');
ylabel('Relative Intensity');
```

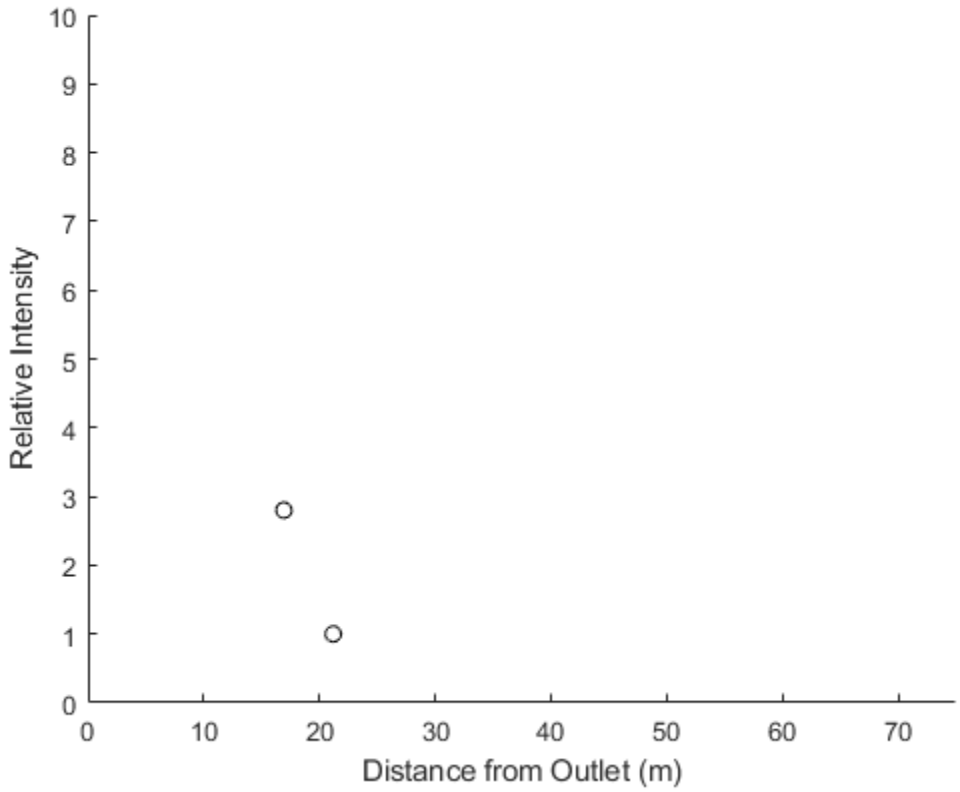

Load Velocity-Time Data

Import data in place of 'extracted data.xlsx' This data is digitized with 'webplotdigitizer.com' from Aleynik *et. al* (2017).

```
dataX = xlsread('extracted data.xlsx','X'); % Input time data in decimal day
dataY = xlsread('extracted data.xlsx','Y'); % Input Seabed Current Speed (m s^-^1).
```

Plot Speed/Time

```
figure % open new figure window
plot(dataX,dataY,'k'); % 2D line plot
xlabel('Decimal Day');
ylabel('Seabed Velocity (m s^-^1)');
```

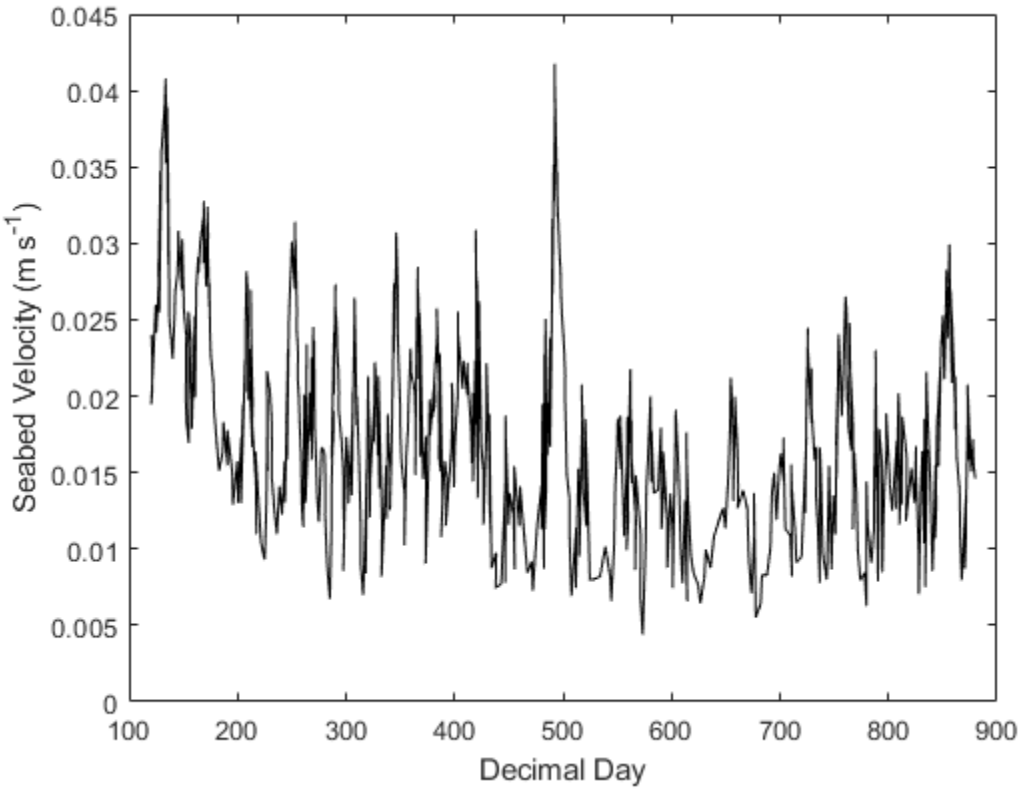

FFT

```
figure
freq = xlsread('extracted data.xlsx','Freq7'); %Freq7 is a vector of frequencies
% 3E-4 (1 every 7 years) and 1 Oscillation per day
F = abs(fft(dataY));% This is the Fast Fourier Transform, it identifies the magnitude of
frequencies in a signal
loglog(freq,F,'k');
grid on;
xlabel('Frequency (Oscillations per Day)');
ylabel('Relative Magnitude');
```

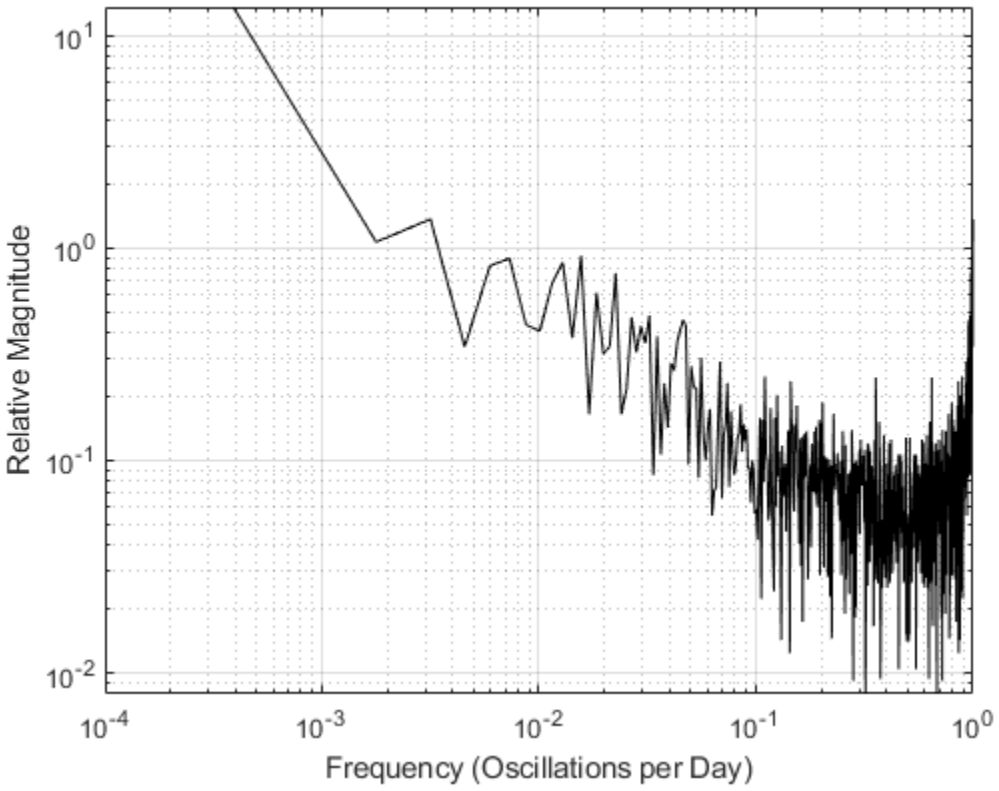

FFT Interpretation

Observing the FFT Figure, interpret the frequency in which "noise" begins (i.e. lowest noise frequency). Input value in inequality

Create velocity model

```
F(freq>0.1)=0;
figure; %open new figure
I = real(ifft(F)); %Produce raw velocity model
I(dataX<130)=0; %IFFT works very strangely on the ends of the x-axis, reduce as far as looks
normal
I(dataX>865)=0; %Increase as far as looks normal
plot (dataX,I,'k');
```

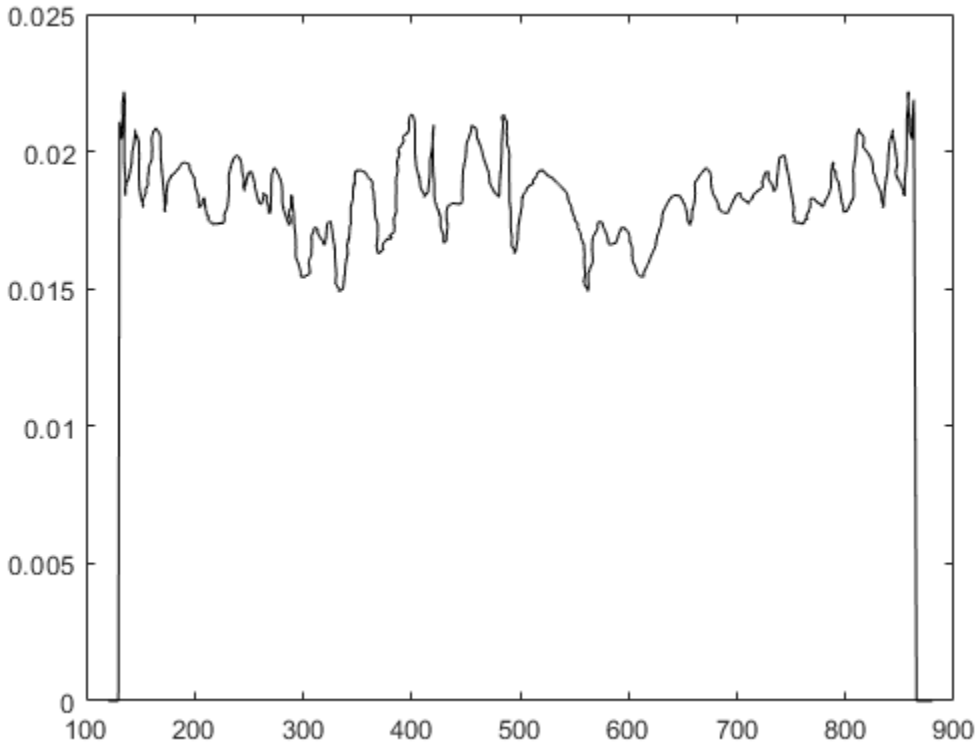

Deduct Settling velocity

```
Mod1 = (I - w1); %Model 1 for Mineral 1
Mod1(Mod1<0)=0; %Ignore negative values
%ModN = I - wN
%ModN(ModN<))=0
plot(dataX,Mod1,'k');
```

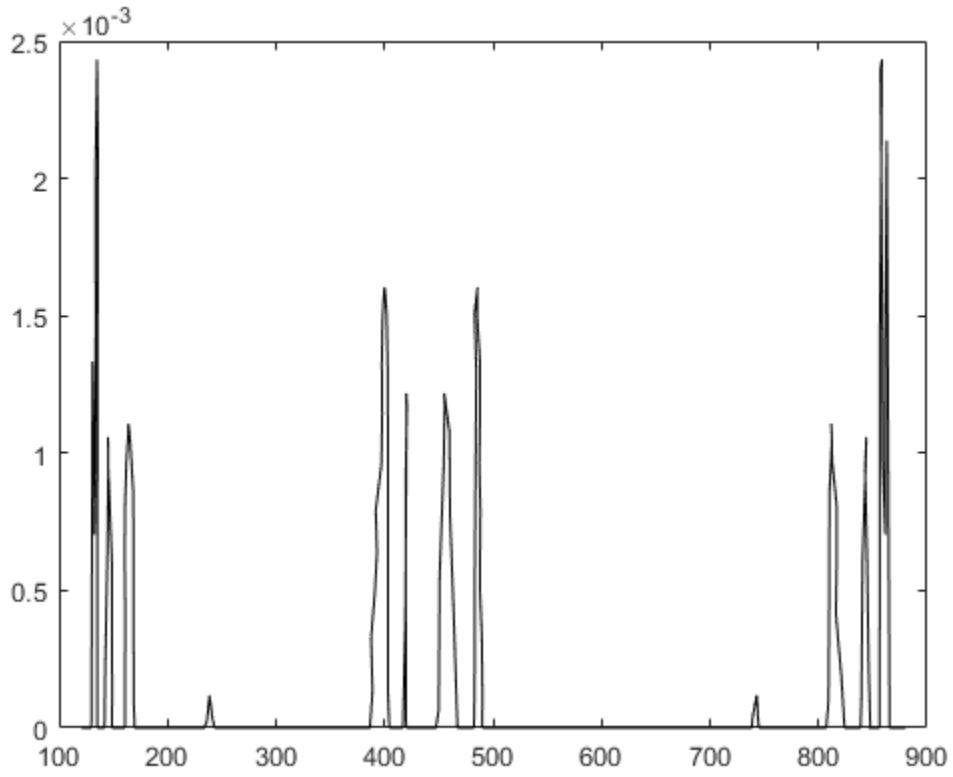

Convert time

```
start = dataX([1]);
S = (dataX - start); %Translate to Days from start
s = 86400*S; %Seconds
```

Integration for PIR_dynamic within PIT

```
figure %open new figure
PIR_1dy=cumtrapz(s,Mod1); %cumulative trapeze method of integration, mineral 1 dynamic
plot (S,PIR_1dy,'k'); %Visulise integration
xlabel('Potential Impact Timeframe (Days)');
ylabel('Potential Impact Range in Dynamic Water (m)');
xlim([0 inf]);
```

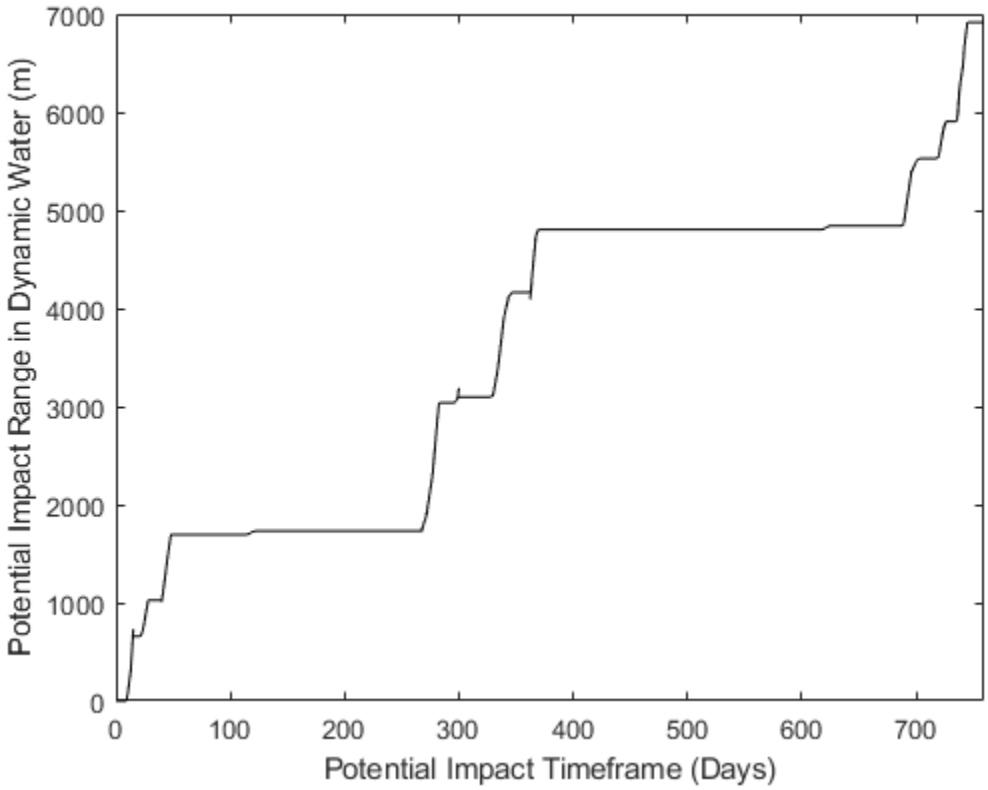

Reiterate Integration for PIR_dynamic within PIT

figure PIR_Ndy=cumtrapz(s,ModN) plot (S,PIR_Ndy,'k'); xlabel('Potential Impact Timeframe (Days)'); ylabel('Potential Impact Range in Dynamic Water (m)'); xlim([0 inf]);

PIR in PIT

PIT = VALUE (Cannot find a way to do this automatically, use data cursor on each plot)
PIR1 = %<Value>, m

```
m1 = a1*A1;
% PIR2 = %<Value>, m
m2 = a2*A2;
% ...
%PIRN = <Value>, m
%mN = aN*AN
```

Plot PII

xdy=[PIR1,PIR2,... PIRN]
ydy=[m1,m2,... mN]
plot(xdy,ydy);
ylabel('Relative Intensity')
xlabel('Distance from outlet')

Published with MATLAB® R2018a